Reflectance Calibration with Normalization Correction in Hyperspectral Imaging

Ines A. Cruz-Guerrero
Facultad de Ciencias
Universidad Autonoma de San Luis Potosi
San Luis Potosi, Mexico
ORCID:0000-0001-8034-8530

Raquel Leon
Institute for Applied Microelectronics
University of Las Palmas de Gran Canaria
Las Palmas de Gran Canaria, Spain
ORCID:0000-0002-4287-3200

Liliana Granados-Castro
Facultad de Ciencias
Universidad Autonoma de San Luis Potosi
San Luis Potosi, Mexico
ORCID:0000-0002-6301-9062

Himar Fabelo
Institute for Applied Microelectronics
University of Las Palmas de Gran Canaria
Las Palmas de Gran Canaria, Spain
ORCID:0000-0002-9794-490X

Samuel Ortega
Norwegian Institute of Food
Fisheries and Aquaculture Research
Tromsø, Norway
ORCID:0000-0002-7519-954X

Daniel U. Campos-Delgado
IICO/Facultad de Ciencias
Universidad Autonoma de San Luis Potosi
San Luis Potosi, Mexico
ORCID:0000-0002-1555-0131

Gustavo Marrero Callico
Institute for Applied Microelectronics
University of Las Palmas de Gran Canaria
Las Palmas de Gran Canaria, Spain
ORCID:0000-0002-3784-5504

Abstract—Today, hyperspectral (HS) imaging has become a powerful tool to identify remotely the composition of an interest area through the joint acquisition of spatial and spectral information. However, like in most imaging techniques, unwanted effects may occur during data acquisition, such as noise, changes in light intensity, temperature differences, or optical variations. In HS imaging, these problems can be attenuated using a reflectance calibration stage and optical filtering. Nevertheless, optical filtering might induce some distortion that could complicate the posterior image processing stage. In this work, we present a new proposal for reflectance calibration that compensates for optical alterations during the acquisition of an HS image. The proposed methodology was evaluated on an HS image of synthetic squares of various materials with specific spectral responses. The results of our proposal show high performance in two classification tests using the K-means algorithm with 97% and 88% accuracy; in comparison with the standard reflectance calibration from the literature that obtained 77% and 64% accuracy. These results illustrate the performance gain of the proposed formulation, which besides maintaining the characteristic features of the compounds within the HS image, keeps the resulting reflectance into fixed lower and upper bounds, which avoids a post-calibration normalization step.

Index Terms—Hyperspectral imaging, optical filters, reflectance calibration

I. Introduction

Hyperspectral (HS) imaging has emerged as a high potential characterization tool, since it is a non-invasive and non-ionizing technique that combines spectroscopy and digital imaging. In HS imaging, the spatial and spectral information of a given scene is captured simultaneously [1]–[3]. This technique was originally developed by spatial agencies for remote sensing, and it has been applied in diverse fields, such as geology [4], archaeology [5], art conservation [6], vegetation monitoring [7], water resources [8], food quality and safety control [9], forensics [10], medical diagnosis [1], etc. In HS imaging, a light source is projected onto the scene of interest, and the incident light is reflected. This reflection process is influenced by various effects such as scattering, diffraction, and absorption, which are influenced by the characteristics of the surface to be analyzed [2], [5], [9]. This information is obtained through a spectral camera, which captures the spectral response of the area of interest in a HS image or hypercube. Therefore, the HS image is a set of two-dimensional images acquired along the electromagnetic spectrum at a given time [2].

In a HS image, each pixel in the two-dimensional spatial plane represents its reflectance curve or spectral signature. These signatures are similar to the fingerprints of the components present in the area of interest. Thus, the characterization of these fingerprints allows us to identify the presence and composition of the scene [1], [2]. However, it is necessary to

process the HS image to determine the elements that make up the analyzed surface. The reason for this is that certain factors may be present at the acquisition time, which can alter the characteristics of the spectral signatures, such as changes in temperature due to the illumination system and in the brightness caused by fluctuation of the input power of the illumination source or its aging [3], [11], [12]. To reduce the impact of these factors that may degrade the characteristics of spectral signatures, a calibration step is applied to the HS images in almost all studies involving this technology in the literature [2].

The calibration stage, in addition to compensating for most adverse effects at the acquisition time, establishes an amplitude range for spectral signatures expressed in percentages [12]. This allows for a standardization of the spectral signatures, i.e., spectral information captured of the same object/component by different HS cameras is consistent in morphology in both scenarios. The standard calibration process, performed in most of the HS image studies, is done by applying a linear transformation to the raw HS image ($I_{raw}(x,y,n) \in \mathbf{R}^{X \times Y \times N}$) with original reflectance signatures:

$$\hat{I}(x,y,n) = 100 \times \frac{I_{raw}(x,y,n) - R_D(x,y,n)}{R_W(x,y,n) - R_D(x,y,n)} \quad (1)$$

where $\hat{I}(x,y,n) \in \mathbf{R}^{X \times Y \times N}$ is the reflectance calibrated HS image with spatial dimensions $X \times Y$ and N number of spectral bands, and $R_D(x,y,n) \in \mathbf{R}^{X \times Y \times N}$ and $R_W(x,y,n) \in \mathbf{R}^{X \times Y \times N}$ are the dark (dark current) and white reference HS images, respectively. Usually, $R_W(x,y,n)$ is obtained from a standard white reference tile, and $R_D(x,y,n)$ by keeping the camera shutter closed. Equation (1) is derived from the spectral response of the sensors, as described in [13], and applies an inverse-model perspective to compensate the non-uniform gain. Thus, this standard calibration process provides consistent spectral signatures for the acquisitions made with different HS cameras and scenarios with the same components

Despite the advantages of the calibration process shown in (1), there are still intricate problems with the HS image capture stage. So the standard transformation in (1) does not fully compensate for the effects caused by the optical filters used in HS camera sensors. Optical filters are used as band-pass components, limiting the acquisition to specific wavelengths and rejecting unwanted information [14]. However, the fundamental properties of band-pass filters in conjunction with electronics can cause some parasitic effects such as crosstalk, leakage, and harmonics, causing the sensors to measure the light of unwanted wavelengths, resulting in a slight change in shape and an increase in the amplitude of the spectral signatures [14], [15]. Nonetheless, the effect of harmonics continues to be considered in the measurements, which primarily affects the amplitude of the spectral signatures and its impact varies depending on the analyzed material [14]. In most cases, the effects of harmonics go unappreciated, because the HS cameras return the discretized spectral response for each pixel [14]. Nonetheless, it is possible to see the impact by comparing the white reference with measurements made under

the same capture conditions. Consequently, there is an increase in variability and sometimes a change in the morphology of the reflectance spectral signatures.

In this context, we present a modification of the reflectance calibration described in (1), which largely compensates for the impact of unwanted alterations in the amplitude of the spectral signatures. The proposed formulation includes a normalization correction, thus ensuring a resulting reflectance in the range zero to one hundred, and thus avoiding the need for a subsequent normalization step. In addition, the proposed calibration decreases the variability and preserves the shape of the spectral signatures, which allows grouping or classifying the spectral signatures of different compounds more accurately.

II. METHOD

The proposed method departs from the raw HS image ($I_{raw}(x,y,n)$), and the dark ($R_D(x,y,n)$) and white ($R_W(x,y,n)$) references, which are used in the standard reflectance calibration. The proposed reflectance calibration is motivated by (1), but defines two auxiliary image

$$\alpha(x,y,n) = I_{raw}(x,y,n) - R_D(x,y,n) \quad (2)$$

$$\beta(x,y,n) = R_W(x,y,n) - R_D(x,y,n) - \min_{x,y,n} \alpha(x,y,n), \quad (3)$$

where $\alpha(x,y,n)$ and $\beta(x,y,n)$ are the numerator and denominator of (1). In $\beta(x,y,n)$, a component is added, which is the general minimum of $\alpha(x,y,n)$, and it is subtracted by applying an offset to the spectral signals in the denominator of (1); this component is used to guarantee that the minimum values are equal to or greater than zero. Subsequently, the same operation is applied to $\alpha(x,y,n)$ to correct for possible negative values caused by unwanted effects at the acquisition stage. It is necessary to clarify that in an ideal case, the global minimum value of $\alpha(x,y,n)$ is greater than or equal to zero, and therefore the smallest values of the spectral signatures are assigned to zero, even in cases with negative values.

Once $\alpha(x,y,n)$ and $\beta(x,y,n)$ have been defined, we apply a normalization step by

$$\hat{\beta}(x,y,n) \triangleq \frac{\beta(x,y,n)}{\max_{x,y}(\beta(x,y,n))} \in [0,1], \quad (4)$$

this operation limits the lower and upper values in $\hat{\beta}(x,y,n)$ to zero and one, respectively. Hence, the role of $\hat{\beta}(x,y,n)$ is to quantify the non-uniform gain over the analyzed wavelengths in a normalized and positive fashion. On the other hand, $\alpha(x,y,n)$ is modified with the same perspective such that

$$\hat{\alpha}(x,y,n) \triangleq \frac{\alpha(x,y,n) - \min_{x,y,n} \alpha(x,y,n)}{\hat{\beta}(x,y,n)}, \quad (5)$$

where the offset is applied using the general minimum of $\alpha(x,y,n)$, restricting the minimum allowable values to zero but not limiting the maximum values ($\hat{\alpha}(x,y,n) \in [0,\infty)$). Finally, the proposed calibration formula is defined as

$$\hat{I}(x,y,n) = 100 \times \frac{\hat{\alpha}(x,y,n)}{\max_{x,y}(\hat{\alpha}(x,y,n))} \in [0,100], \quad (6)$$

thus establishing the upper limit of the spectral signatures within the image $\hat{I}(x, y, n)$ and ensuring values in the range of [0,100]. Once more, the proposed methodology, as in (1), looks to compensate for the non-uniform gain of the HS sensor, but now limiting the resulting values in (6). This new perspective reduces the spectral variability and allows more accurate classification results, as will be shown next.

III. RESULTS

This section presents the comparison results between the standard calibration (SC), and the proposed calibration (PC) in this work. The two approaches have been evaluated on an HS image, whose acquisition, characteristics, and discussion of results are described in the following subsections. Our evaluations were conducted in MATLAB®2018a on a computer with a 4.2 GHz Intel Core i7 quad-core processor and 16 GB of RAM.

A. Database Description

The evaluation of PC and SC was performed on an HS image of ten squares of synthetic material (enumerated from S1 to S10) and four different colors (white, black, red, and magenta). The test-bench has three main materials: polylactic acid (PLA), acrylonitrile butadiene styrene (ABS), and polyethylene terephthalate glycol (PETG). These materials have been used in several studies for the characterization and development of HS techniques [16]. The test-bench materials in this work can be seen in Fig. 1, where at the top is a standard 99% Spectralon White diffuse reflectance material used to obtain the white reference tile $R_W(x, y, n)$. At the bottom section, there are PLA (S2, S5, and S6), ABS (S1, S8, S9, and S10), and PETG (S3, S4, and S7), corresponding to the colors white (S1 and S4), magenta (S2, S8, and S10), red (S3, S6, and S9), and black (S5 and S7).
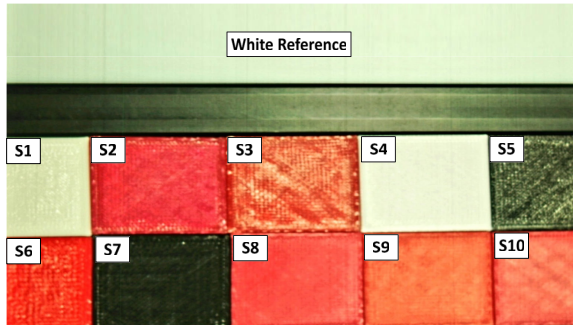
Fig. 1. Materials of the test-bench used for the evaluation of the SC and PC methodologies. The standard 99% Spectralon White diffuse reflectance material utilized to obtain the white reference tile $R_W(x, y, n)$ is presented at the top. In the bottom part of the image, there are ten plastic squares which have different colors and are composed of three materials: polylactic acid (PLA), acrylonitrile butadiene styrene (ABS), and polyethylene terephthalate glycol (PETG).

In order to obtain the HS image, we used a visible and near-infrared (VNIR) push-broom camera (Hyperspec® VNIR A-Series, Headwall Photonics Inc, MA, USA); in conjunction
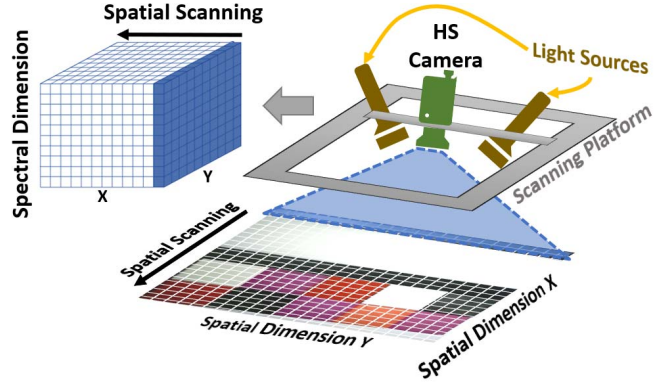
Fig. 2. Diagram of HS image acquisition system.

with a scanning platform to shift the camera field of view to obtain the second spatial dimension. In addition, a dedicated illumination system capable of emitting cold light in the spectral range between 400 and 2200 nm is attached to the system. A 150 W QTH (quartz tungsten halogen) light source was coupled to a cold light emitter employing a fiber optic cable that avoids the high temperatures produced by the lamp on the surface to be analyzed. The general diagram of the HS image acquisition system is shown in Fig. 2, as well as an example of how the images are structured.

The HS image of the test-bench was acquired by simultaneously capturing the white reference and the plastic squares in Fig. 1. Therefore the resulting raw HS image $(I_{raw}(x, y, n))$ consists of 440×1004 spatial pixels with 826 spectral bands between 400 to 1000 nm. In addition, the dark reference $(R_D(x, y, n))$ was captured in all the area of interest $(440 \times 1004$ spatial dimension), while the white reference $(R_W(x, y, n))$ was established as a vector of 1004 pixels with 826 spectral bands by averaging the vectors corresponding to the reflecting surface in Fig. 1. Because the push-broom camera performs line capture, the spectral response along the columns is approximately the same, so averaging decreases the variation and smooths the reference spectral signatures.

B. Results of Calibration

The evaluation of both SC in (1) and PC in (6) methods on the test-bench can seen in Fig. 3, where each row represents the spectral information of each square. The first and second columns show the results of the SC and PC spectral signatures, respectively. Hence, SC shows values higher than 100%, having scenarios like the one in S1, in which practically all the spectral signatures are above 100%. On the other hand, the PC results remain within the expected range [0, 100] with a lower dispersion of the spectral signatures, compared to the SC results. All the results of both calibrations were corroborated when analyzing the third column, where the means and standard deviations (SDs) of PC remain below 100%. In contrast, the means and SDs of SC exceed 100%, with the exception of squares S5 and S7. The SDs show a decrease in the PC results in all squares compared to SC.

Finally, the fourth column illustrates the mean and SD of the two approaches after performing a preprocessing stage (which is described in depth in [17]); that consists of three steps: (i) extreme band removal and band reduction, (ii) smoothing of spectral signatures, and (iii) normalization. The results in this column show a similar mean and SD between the two methods, with PC performing better in S5 and S7. This behavior is due to the elimination of the end bands, which reduces the variability among the spectral signatures. In fact, there is a large variability at the extremes due to the response of the HS sensors at those wavelengths. Hence, steps (ii) and (iii) reduce the differences between the two methods. However, the normalization in (iii) can also eliminate distinctive features in the information for classification purposes, and it would not be necessary if there were no undesired effects in the capture.

In addition to the above comparison, two classifications were performed on the HS image with both calibration methods without considering the preprocessing stage. This evaluation was carried out by using the standard K-means algorithm [18], with K equal to 4 and 9, and using the Euclidean and the L_1 distances as metrics for each case, respectively. The first case generates a color classification, and the second case a per square classification. The classification results per color with K = 4 are reported in Fig. 4, where the results of the HS image with SC present many errors in most of the squares, and produce an accuracy of 79% (see Fig. 4A). In contrast, the segmentation of the HS image with PC has few errors, which occur mainly in the S3 and S5 squares (see Fig. 4B). As a result, this second classification produces an accuracy of 97%, which is a sustainable improvement compared to the corresponding results with SC.

Figure 5 presents the classification results per square, where in general, there is an increase in the classification errors with respect to the per color case; this is due to the similarity between the spectral signatures and a certain level of texture of the squares in the test-bench. The results with SC are presented in Fig. 5A, which shows an increase in classification errors among the labels assigned to the different squares especially in S2, S3, S6, and S10. Furthermore, S10 is classified completely with the S5 label, and this last one is predominantly classified with the label S9. Likewise, Fig. 5B reports the classification results with PC, which shows a decrease in classification errors in contrast to Fig. 5A. Hence, the squares with the highest coincidence were S2, S3, and S5. Therefore, S10 and S8 were correctly classified with the same label because both squares are of the same material and color. This classification yields 64% and 88% accuracy overall for SC and PC classification, respectively. Consequently, in this second evaluation, once again the PC method showed a significant improvement over SC.

Performing the classification tests on the calibrated data in conjunction with the preprocessing stage generates highly similar results for both SC and PC spectral signatures. The color classification results are presented in Fig. 6, where most mistakes are found mainly in S1 and S5, with a higher noise level in the case of PC in these squares. On the other hand, the remaining squares with PC present a lower noise level than in the case of SC. The latter corroborated when analyzing the overall classification accuracy, in which PC generates 90% while SC is 89%. This behavior repeats itself in the classification per square, as shown in Fig. 7, improving accuracy in the case of PC with an accuracy of 69%, in contrast to the results produced by SC that generate an accuracy of 64%.

In addition to the above tests, a classification test with both calibrations is evaluated in conjunction with the preprocessing step but without considering the zero-to-one normalization; in order to verify that the normalization is the cause of the similarity in the shape of the spectral signatures. Qualitatively, these results are very similar to those presented in Figs 4 and 5 for both SC and PC. On the other hand, when analyzing the quantitative accuracy data, 79% and 95% are produced for SC and PC color classification. While in the case of square classification 64% and 87% are generated for SC and PC, respectively. Thus, there is a slight decrease in PC compared to the classification results with only the calibration step, while SC remains constant in both tests.

To generate a deeper analysis of the results obtained in this evaluation, a dimensional reduction was performed to three-dimensional points of each calibrated spectral signature through the locally linear embedding (LLE) algorithm [19]. The LLE algorithm is a dimensionality reduction method that looks to preserve the geometrical characteristics of the original manifold by considering the information of neighboring points. The LLE evaluation was performed considering five neighbors for reduction and estimating the nearest neighbors using the KDTree algorithm [20]. The selection of LLE was made by comparing with PCA and t-SNE [21]. PCA and t-SNE generated qualitatively less class separation in a 3-dimensional space when evaluating the data with both calibrations. Meanwhile, LLE allowed for a reduction in high-dimensional space by detecting non-linear structures while preserving the geometrical characteristics of the original data [21].

The results of the dimensional reduction are presented in Fig. 8, where Fig. 8A and Fig. 8B show the SC and PC reductions, respectively, while Fig. 8C and Fig. 8D display the SC and PC dimensional reductions after applying the preprocessing step described above. In the figures with SC dimensional reductions, the data accumulated in a central region with a high intercept among data from different squares. Meanwhile, the results in the PC data showed a higher separability in each square. This property justified the behavior of both calibrations in the previous classification tests. On another side, when analyzing the reductions with the preprocessing stage, the dimensional reduction with PC keeps a shape consistent with Fig. 8B, maintaining the proportions in the three dimensions and decreasing the outliers of each square. As in the previous case, in the dimensional reduction of the SC data and preprocessing, the outliers are somewhat reduced and the data are condensed into sharper curves than in the case of Fig. 8A. However, when applying the normalization of zero to one, a transformation is performed on the calibrated spectral
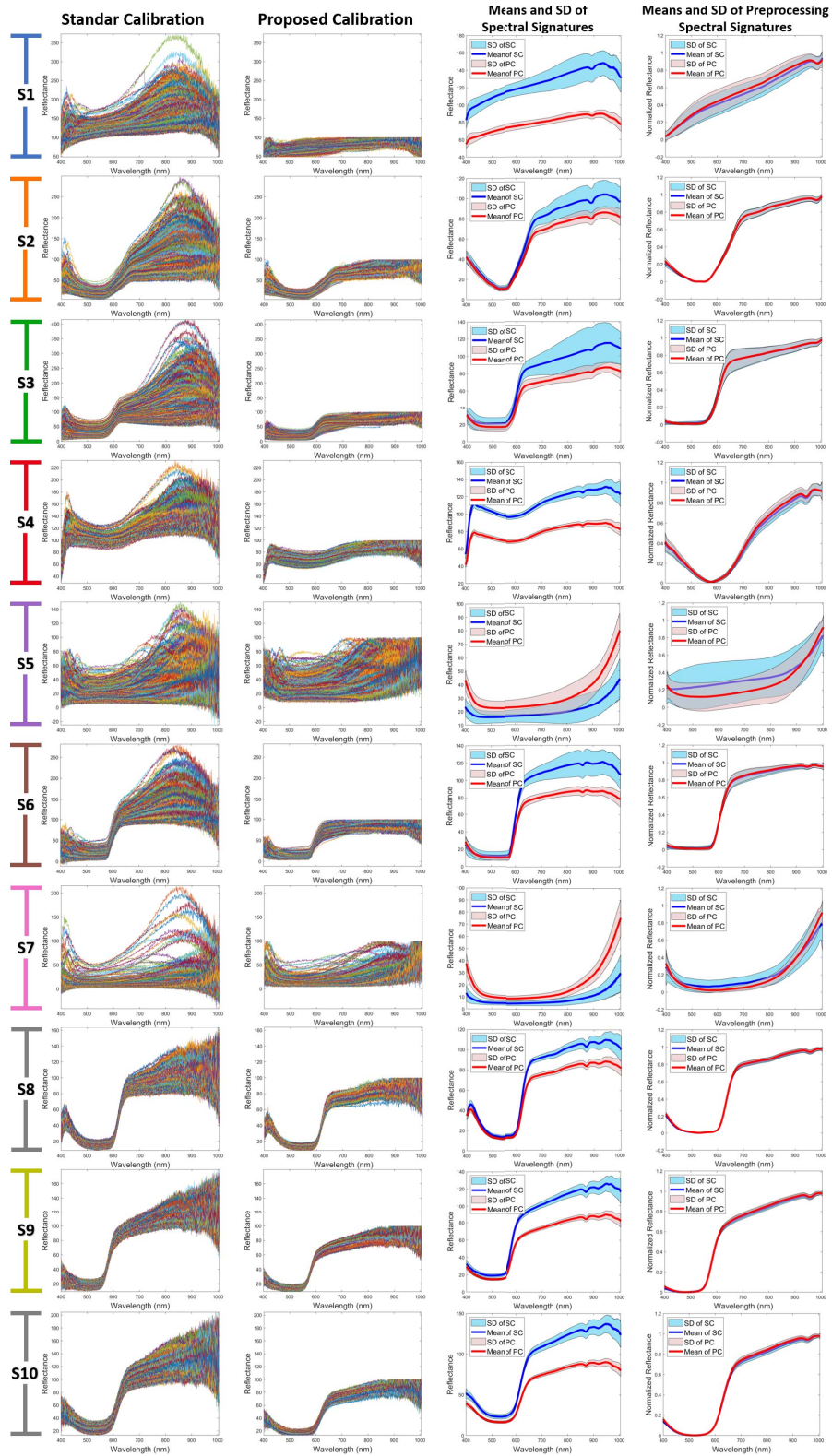
Fig. 3. Results of calibration of the HS image with the test-bench, where each row represents the spectral information of each square. The first column shows the results of the standard calibration (SC), while the second column presents the results of the proposed calibration (PC). The third column reports the mean and standard deviation of both approaches. Finally, the fourth column also shows the mean and standard deviation of both methods after performing a preprocessing step.
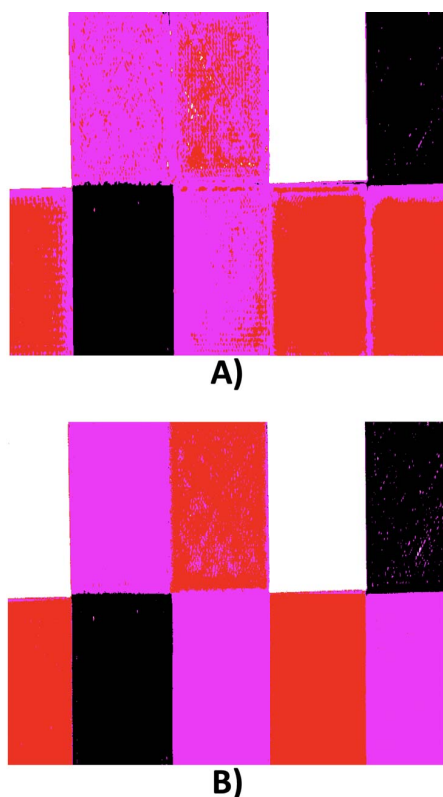
Fig. 4. Classification results per color. A) standard calibration and B) proposed calibration.

Fig. 5. Classification results per square. A) standard calibration and B) proposed calibration.

signatures; this produces a similar behavior in both SC and PC, causing the data to concentrate and intercept in a central area, explaining the behavior shown in the fourth column of Fig. 3. When the classification is performed with the preprocessing stage, the results are very similar. In brief, at least in the case of PC, where a normalization step is not necessary, given the limitation posed in the formulation; the application of this transformation modifies the spectral signatures losing characteristics that allows generating a correct identification of the data of each square and therefore a more accurate classification.

IV. CONCLUSIONS

This paper presents a new formulation for reflectance calibration in HS images, which compensates for some of the undesired effects in the image acquisition stage. Our results show that the proposed calibration maintains the shape of the spectral signatures, limits their amplitudes in the range 0 to 100%, and allows a larger separability among the classes present in the HS image. As a future work, we will evaluate the proposal under different illumination levels and interference from other light sources, to check the performance under adverse scenarios during the data acquisition stage. Furthermore, we will identify the diverse components that affect the acquisition of the HS images to propose specific models to mitigate these negative effects.

REFERENCES

[1] G. Lu and B. Fei, "Medical hyperspectral imaging: a review," *Journal of biomedical optics*, vol. 19, no. 1, p. 010901, 2014.
[2] M. J. Khan, H. S. Khan, A. Yousaf, K. Khurshid, and A. Abbas, "Modern trends in hyperspectral image analysis: A review," *Ieee Access*, vol. 6, pp. 14118–14129, 2018.
[3] A. Noviyanto and W. H. Abdulla, "Segmentation and calibration of hyperspectral imaging for honey analysis," *Computers and Electronics in Agriculture*, vol. 159, pp. 129–139, 2019.
[4] F. D. Van der Meer, H. M. Van der Werff, F. J. Van Ruitenbeek, C. A. Hecker, W. H. Bakker, M. F. Noomen, M. Van Der Meijde, E. J. M. Carranza, J. B. De Smeth, and T. Woldai, "Multi-and hyperspectral geologic remote sensing: A review," *International Journal of Applied Earth Observation and Geoinformation*, vol. 14, no. 1, pp. 112–128, 2012.
[5] C. Cucci, M. Picollo, L. Chiarantini, G. Uda, L. Fiori, B. De Nigris, and M. Osanna, "Remote-sensing hyperspectral imaging for applications in archaeological areas: Non-invasive investigations on wall paintings and on mural inscriptions in the pompeii site," *Microchemical Journal*, vol. 158, p. 105082, 2020.
[6] C. Cucci and A. Casini, "Hyperspectral imaging for artworks investigation," in *Data Handling in Science and Technology*, vol. 32, pp. 583–604, Elsevier, 2020.
[7] T. Ishida, J. Kurihara, F. A. Viray, S. B. Namuco, E. C. Paringit, G. J. Perez, Y. Takahashi, and J. J. Marciano Jr, "A novel approach for vegetation classification using uav-based hyperspectral imaging," *Computers and electronics in agriculture*, vol. 144, pp. 80–85, 2018.
[8] R. Abdlaty, M. Gobara, I. Naiem, and M. Mokhtar, "Innovative technique for analysis of wastewater contaminants using hyperspectral imaging," *Journal of Spectral Imaging*, vol. 9, 2020.
[9] H. Huang, L. Liu, and M. O. Ngadi, "Recent developments in hyperspectral imaging for assessment of food quality and safety," *Sensors*, vol. 14, no. 4, pp. 7248–7276, 2014.
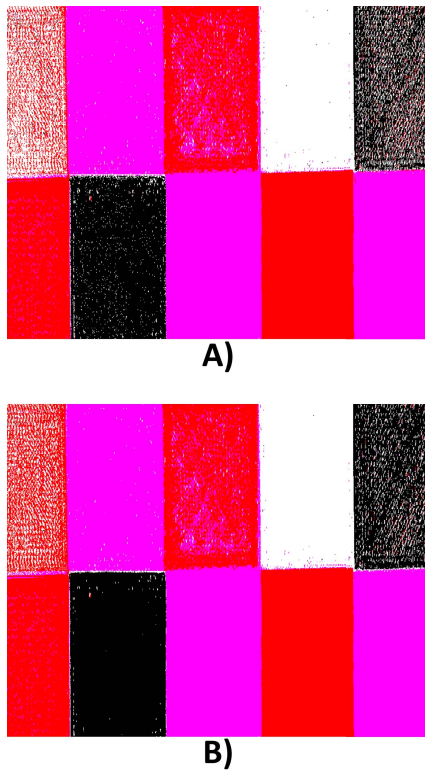
Fig. 6. Classification results per color with preprocessing stage. A) standard calibration and B) proposed calibration.
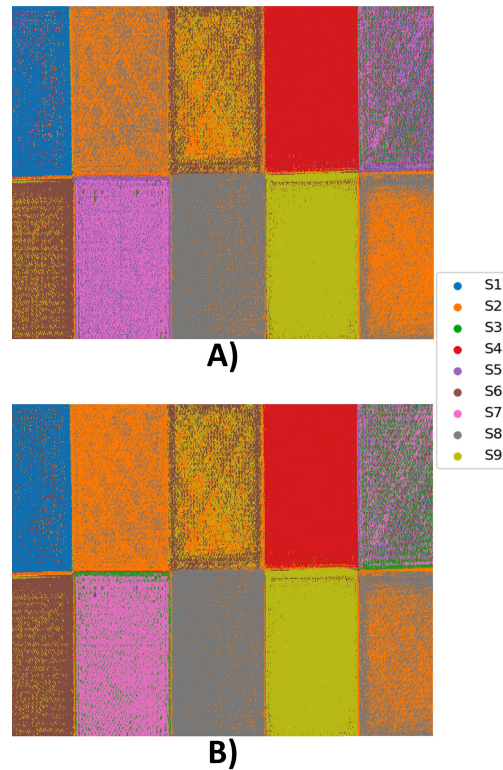
Fig. 7. Classification results per square with preprocessing stage. A) standard calibration and B) proposed calibration.

[10] M. Á. F. de la Ossa, J. M. Amigo, and C. García-Ruiz, "Detection of residues from explosive manipulation by near infrared hyperspectral imaging: A promising forensic tool," *Forensic science international*, vol. 242, pp. 228–235, 2014.

[11] R. Koprowski, S. Wilczyński, Z. Wróbel, and B. Błońska-Fajfrowska, "Calibration and segmentation of skin areas in hyperspectral imaging for the needs of dermatology," *Biomedical Engineering Online*, vol. 13, no. 1, pp. 1–19, 2014.

[12] P. Geladi, J. Burger, and T. Lestander, "Hyperspectral imaging: calibration problems and solutions," *Chemometrics and intelligent laboratory systems*, vol. 72, no. 2, pp. 209–217, 2004.

[13] N. Gat, "Imaging spectroscopy using tunable filters: a review," *Wavelet Applications VII*, vol. 4056, pp. 50–64, 2000.

[14] J. Pichette, T. Goossens, K. Vunckx, and A. Lambrechts, "Hyperspectral calibration method For CMOS-based hyperspectral sensors," in *Photonic Instrum. Eng. IV*, vol. 10110, p. 101100H, SPIE, feb 2017.

[15] J.-B. Thomas, P.-J. Lapray, P. Gouton, and C. Clerc, "Spectral characterization of a prototype sfa camera for joint visible and nir acquisition," *Sensors*, vol. 16, no. 7, p. 993, 2016.

[16] R. Leon, H. Fabelo, S. Ortega, J. F. Piñeiro, A. Szolna, M. Hernandez, C. Espino, A. J. O'Shanahan, D. Carrera, S. Bisshopp, *et al.*, "Vnir–nir hyperspectral imaging fusion targeting intraoperative brain cancer detection," *Scientific reports*, vol. 11, no. 1, pp. 1–12, 2021.

[17] I. A. Cruz-Guerrero, R. Leon, D. U. Campos-Delgado, S. Ortega, H. Fabelo, and G. M. Callico, "Classification of hyperspectral in vivo brain tissue based on linear unmixing," *Applied Sciences*, vol. 10, no. 16, p. 5686, 2020.

[18] M. Ahmed, R. Seraj, and S. M. S. Islam, "The k-means algorithm: A comprehensive survey and performance evaluation," *Electronics*, vol. 9, no. 8, p. 1295, 2020.

[19] B. Ghojogh, A. Ghodsi, F. Karray, and M. Crowley, "Locally linear embedding and its variants: Tutorial and survey," *arXiv preprint arXiv:2011.10925*, 2020.

[20] Y. Chen, L. Zhou, Y. Tang, J. P. Singh, N. Bouguila, C. Wang, H. Wang, and J. Du, "Fast neighbor search by using revised kd tree," *Information Sciences*, vol. 472, pp. 145–162, 2019.

[21] F. Anowar, S. Sadaoui, and B. Selim, "Conceptual and empirical comparison of dimensionality reduction algorithms (pca, kpca, lda, mds, svd, lle, isomap, le, ica, t-sne)," *Computer Science Review*, vol. 40, p. 100378, 2021.
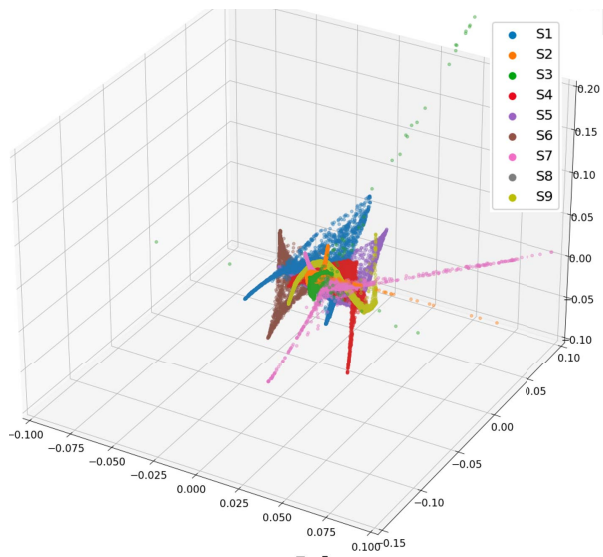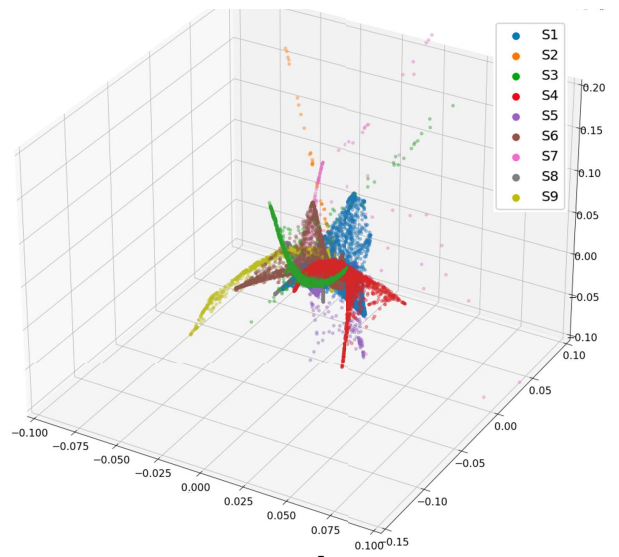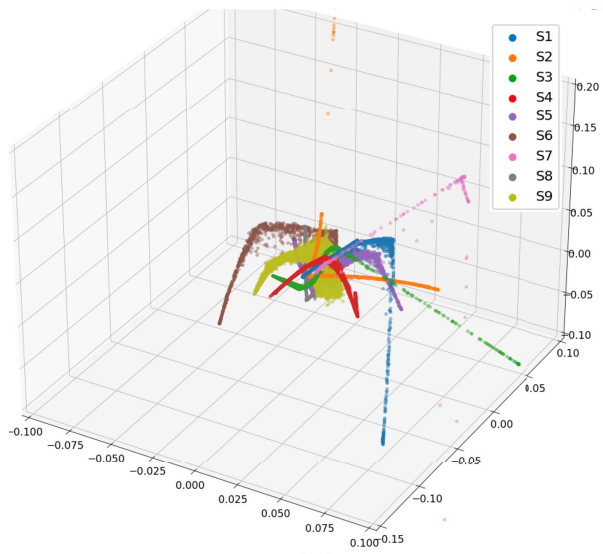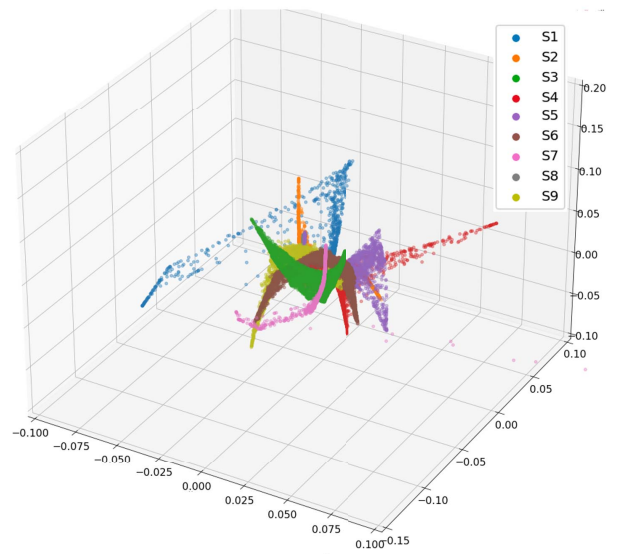
Fig. 8. Dimensional reduction of spectral signatures with: A) standard calibration, B) proposed calibration, C) standard calibration with preprocessing stage, and D) proposed calibration with preprocessing stage.